**Interdisciplinary Research in Medical Sciences Specialty**
**ISSN: 3062-4401**
2025, Volume 5, Issue 1, Page No: 240-259

Available online at: www.galaxypub.co/page/journals

**Galaxy Publication**

# piR-hsa-164586 Orchestrates Tumor Microenvironment Reprogramming and Metastatic Progression in NSCLC Revealed by Single-Cell Transcriptomics

**Sofía Martínez[1]*, Carlos Gómez[1], Lucia Navarro[2]**

[1]Department of Single-Cell Genomics and Tumor Microenvironment, Faculty of Medicine, Polytechnic University of Madrid, Madrid, Spain.
[2]Department of Non-Coding RNA and Metastasis Research, Faculty of Medicine, University of Barcelona, Barcelona, Spain.

***E-mail** ✉ sofia.martinez@upm.es

**Received:** 12 April 2025; **Revised:** 20 June 2025; **Accepted:** 24 June 2025

## ABSTRACT

The identification of tumor-specific markers combined with targeted therapeutic approaches has yielded substantial clinical benefits in recent years. PIWI-interacting RNAs (piRNAs), which exert important influences on tumor development, hold considerable promise as targets for creating molecular agents against cancer. This investigation confirmed the capacity of piR-hsa-164586 to promote invasion and metastasis in non-small cell lung cancer (NSCLC) cells. Building upon earlier findings of its markedly elevated levels in NSCLC tissues and serum extracellular vesicles, the study employed both in vitro and in vivo models to substantiate this role. By integrating single-cell RNA sequencing (scRNA-seq) with supplementary molecular analyses, the work showed that elevated expression of piR-hsa-164586 modifies the tumor microenvironment in NSCLC through enrichment of mesenchymal features in tumor epithelial cells. In addition, piR-hsa-164586 participates in controlling the PI3K-AKT signaling cascade and epithelial–mesenchymal transition, which in turn accelerates the invasive and metastatic spread of NSCLC cells. The non-PIWI protein MYH9 interacts directly with piR-hsa-164586, and reduced expression of either molecule correlates with more positive outcomes in NSCLC. Overall, the findings delineate the precise mechanism through which piR-hsa-164586 functions as a tumor marker in NSCLC while offering critical support for the design of molecularly targeted treatments for this malignancy.

**Keywords:** Microenvironment, MYH9, NSCLC, piRNAs, Single-cell RNA sequencing

**How to Cite This Article:** Martínez S, Gómez C, Navarro L. piR-hsa-164586 Orchestrates Tumor Microenvironment Reprogramming and Metastatic Progression in NSCLC Revealed by Single-Cell Transcriptomics. Interdiscip Res Med Sci Spec. 2025;5(1):240-59. https://doi.org/10.51847/GpmDbp4quO

## Introduction

As reported by the International Agency for Research on Cancer (IARC), non-small cell lung cancer (NSCLC) belongs to the group of malignancies characterized by the greatest incidence and mortality [1]. Even with the application of combined radiotherapy, chemotherapy, and immunotherapy, individuals diagnosed with advanced NSCLC typically face unfavorable survival rates [2], primarily because of the aggressive invasive and metastatic behavior exhibited by the malignant cells [1, 3]. Gene-targeting approaches have recently gained prominence within precision medicine, creating fresh prospects for improving longevity in patients with late-stage NSCLC [4-6].

Small non-coding RNAs (sncRNAs), particularly microRNAs (miRNAs), have thus far achieved only modest success in tumor-directed treatments, mainly owing to constraints regarding specificity, effective delivery, and patient tolerability [7, 8]. In contrast, PIWI-interacting RNAs (piRNAs) are viewed as potentially superior candidates for anti-tumor strategies compared with miRNAs [9]. piRNAs constitute a class of sncRNAs spanning 24 to 31 nucleotides that commonly associate with PIWI proteins to repress transposons, thereby contributing to multiple cellular processes such as tumor cell invasion and distant spread [9, 10]. Notably, piRNAs can enhance

metastatic potential by altering gene expression patterns, modifying epigenetic landscapes, and engaging key signaling routes that stimulate migration, tissue invasion, and colonization in various cancer types [10-14]. Crucially, piRNAs demonstrate strong cellular and genetic specificity. Their 2′-O-methylation at the 3′ end improves delivery characteristics and reduces immunogenicity. These properties [9, 15] therefore suggest piRNAs as strong candidates for future development into advanced tumor-targeting molecular pharmaceuticals.

While studies have addressed piRNA-mediated regulation in breast, liver, and colorectal cancers [16-22], the detailed molecular processes governing piRNA activity in NSCLC progression are still largely unclear, which has hindered progress toward targeted drug development. Previous analyses identified pronounced upregulation of piR-hsa-164586 in NSCLC tissues and circulating extracellular vesicles, along with a significant association with Tumor-Node-Metastasis (TNM) stage. This evidence positions piR-hsa-164586 as a candidate therapeutic target for controlling NSCLC metastasis and a central element in anti-NSCLC pharmaceutical research [23].

The present work represents the first comprehensive validation of piR-hsa-164586's involvement in driving NSCLC invasion and metastasis using complementary in vitro and in vivo experimental systems. Through the combined application of single-cell RNA sequencing (scRNA-seq) and other molecular tools, the study established that overexpression of piR-hsa-164586 perturbs the tumor niche in NSCLC by expanding mesenchymal subpopulations within lung adenocarcinoma epithelial cells (LUAD_ECs). The investigation also provided initial demonstration that piR-hsa-164586 modulates the PI3K-AKT pathway as well as epithelial-mesenchymal transition (EMT) processes, thereby hastening the invasive and metastatic capabilities of NSCLC cells. These effects are intimately connected to the physical association between piR-hsa-164586 and myosin heavy chain 9 (MYH9, a non-PIWI protein). Moreover, experimental reduction of either piR-hsa-164586 or MYH9 was strongly linked to enhanced clinical prognoses among NSCLC patients. In conclusion, this research clarifies the distinctive contribution of piR-hsa-164586 to remodeling the tumor microenvironment and advancing metastatic progression in NSCLC, thereby furnishing an essential platform for future development of piR-hsa-164586-directed molecular therapies.

## Materials and Methods

### *Cell culture*

The cell lines BEAS-2B, A549, and HCC2279 were obtained and maintained according to previously reported protocols [24].

### *RNA extraction and RT-qPCR*

Total RNA was isolated from BEAS-2B, A549, and HCC2279 cells, and gene expression levels were quantified by RT-qPCR following established procedures [24].

### *Reverse transcription at low dNTP concentrations followed by PCR (RTL-P)*

RNA isolation, denaturation, 3′-hydroxy end ligation, reverse transcription, PCR amplification, and electrophoretic analysis of products were conducted as previously described [24].

### *Fluorescence in situ hybridization*

Fluorescence in situ hybridization (FISH) was utilized to assess the subcellular localization of piR-hsa-164586 in A549 and HCC2279 cells, performed according to the published protocol [24]. A Cy3-conjugated RNA probe specific for piR-hsa-164586 (sequence 5′-3′: GCAGCTAATGGAATTCAGTTCTCA) was designed and synthesized by GenePharma (Shanghai, China).

### *Cell transfection*

#### *Transfection of agomir and antagomir*

To evaluate the biological impact of piR-hsa-164586, A549 and HCC2279 cells were transfected with custom-designed agomir and antagomir constructs synthesized by GenePharma (Shanghai, China). Cells were plated at a density of $2 \times 10^5$ per well in 6-well plates and grown to 50%–70% confluence. Prior to transfection, culture medium was replaced with serum-free medium. Transfection complexes were prepared by separately incubating piR-hsa-164586 agomir, agomir scramble control (Ago-NC), antagomir, or antagomir scramble control (Ata-NC) with serum-free medium and Lipofectamine 3000 (Thermo Fisher, USA) with serum-free medium. The mixtures

were combined and incubated for 0.5 h at room temperature before addition to cells. Four treatment groups were established: agomir, Ago-NC, antagomir, and Ata-NC. After 6 h, the medium was replaced with complete growth medium, and cells were cultured for an additional 42 h. Transfection efficiency was confirmed by RT-qPCR as previously reported. Transfected cells were subsequently used for EdU incorporation, CCK-8, flow cytometry, wound-healing, and Transwell assays. Detailed protocols are available in Supporting Information S1.

MYH9 serves as the direct binding partner of piR-hsa-164586. Three MYH9-specific siRNAs (si-MYH9-homo-813, si-MYH9-homo-1399, and si-MYH9-homo-3074) along with a negative control were obtained from GenePharma (China). A549 and HCC2279 cells were assigned to four groups: si-MYH9-homo-813 (si-MYH91), si-MYH9-homo-1399 (si-MYH92), si-MYH9-homo-3074 (si-MYH93), and normal control (NC). Transfection was performed under identical conditions, and cells were harvested after 48 h for Western blot and RT-qPCR analyses. Detailed procedures are described in Supporting Information S1.

*Generation of stable cell lines*

This section describes a comprehensive evaluation of piR-hsa-164586 function in NSCLC cells (A549 and HCC2279) achieved through lentiviral vector construction. The lentiviral plasmid was engineered to co-express Green Fluorescent Protein (GFP) and a puromycin resistance gene, enabling reliable tracking and selection of cells with modified piR-hsa-164586 expression. Lentiviral particles were produced and employed to generate three experimental groups: the overexpression (OE) group, the knockdown (KD) group, and the normal control (NC) group in A549 and HCC2279 cells. Twelve hours after transfection, the serum-free medium was replaced with complete culture medium, and cells were incubated for an additional 36 h. Transduced cells were then subjected to selection with 2 μg/mL puromycin for one week. Established stable lines were subsequently maintained in medium supplemented with 0.5 μg/mL puromycin. Transfection efficiency was confirmed by RT-qPCR using the previously described protocol. These stable cells were utilized in downstream assays including flow cytometry, wound healing, and Transwell experiments.

To investigate MYH9 function, a lentiviral plasmid designed for MYH9 knockdown and its corresponding control were designed and produced by GenePharma (China). The si-MYH9-homo-3074 sequence, which demonstrated superior knockdown efficiency, was selected for lentiviral packaging. The transfection and selection procedures mirrored those outlined above. A549 and HCC2279 cells were assigned to two groups: the siMYH9 group (siMYH9) and the normal control group (siNC). Transfected cells were subsequently used for transcriptome sequencing as detailed below.

MYH9-knockout cell lines were generated to further examine the interplay between piRNA and MYH9. CRISPR/Cas9 genome editing was applied to create MYH9-deficient NSCLC lines in A549 and HCC2279 cells. The lentiCRISPR v2 vector (AiJi Bio-tech) harboring Cas9-Flag, sgRNA (sgMYH9: CACGTGCCTCAACGAAGCCT; sgNC: GTATTACTGATATTGGTGGG), and a puromycin resistance cassette was utilized [25]. Cells were plated in 24-well dishes at a density of $3 \times 10^5$ cells per well. Following 12 h of viral transduction (MOI: 20), the medium was refreshed. At 48 h post-infection, cells were selected with 4 μg/mL puromycin [26].

*Xenograft tumor model*

All animal experiments were performed in accordance with the Guide for the Care and Use of Laboratory Animals and were approved by the Experimental Animal Ethics Committee of Qingdao University (protocol ID: QDU-AEC-2022509). Fifteen female BALB/c nude mice (4–6 weeks old) were obtained from Charles River (Beijing, China). The mice were randomly divided into three groups: the overexpression (OE) group, the knockdown (KD) group, and the NC group. Stable OE, KD, and NC A549 cell lines were established using lentiviral transduction followed by puromycin selection. A cell suspension (0.1 mL at $1 \times 10^6$ cells/mL) was injected subcutaneously into the right flank of each mouse. Tumor dimensions were measured every 7 days, and tumor volume was calculated using the formula $(\text{width}^2 \times \text{length})/2$. On day 40, tumor fluorescence intensity was assessed using an in vivo imaging system (IVIS, USA). Tumors were then surgically excised, weighed, and processed for hematoxylin and eosin (H&E) staining, immunofluorescence (IF), multiplex immunofluorescence (MxIF), and immunohistochemistry (IHC). Detailed experimental procedures are provided in Supporting Information S1.

*RNA pull-down assay*

Biotinylated piR-hsa-164586 probes and negative control probes were synthesized by GenePharma (Shanghai, China). A549 and HCC2279 cells were harvested from two 10-cm dishes per experimental group, washed with PBS, and lysed in 2 mL of cell lysis buffer. Cells were scraped and transferred to Eppendorf tubes. Lysates were prepared using an automated focused ultrasound processor, followed by centrifugation at 1500×g for 40 min. The supernatant was collected for subsequent steps. Probes were diluted to a final concentration of 10 μM. Magnetic beads were vortexed thoroughly and separated on a magnetic rack. After washing once with 1 mL of Buffer 1, 500 μL of biotinylated nucleic acid in Buffer 1 was added to the beads and incubated with rotation. The mixture was incubated overnight at 4°C, after which beads were magnetically separated and washed three times to eliminate unbound material. Bound RNA-protein complexes were eluted using a low-salt buffer. Eluted proteins were analyzed by mass spectrometry (MS) and Western blotting to identify specific RNA-interacting partners. MS analysis was performed by Zhongke Xinsheng (Zhejiang) Biotechnology Co., Ltd. to characterize protein targets of the RNA probe. Western blot procedures followed previously established methods.

*Molecular docking*

The secondary structure of piRNA-hsa-164536 (UGAGAACUGAAUUCCAUAGGCUGC) was modeled using Vfold2D [27], while its tertiary structure was generated with Vfold3D. The three-dimensional coordinates of MYH9 were downloaded from the Protein Data Bank (PDB) database [28].

This study applied HDOCK lite v1.1, a sophisticated protein-nucleic acid docking tool that predicts biomolecular associations by combining physical principles with bioinformatics strategies [29]. Owing to the absence of predefined binding site information, the software executed global docking. This involved exhaustive sampling of all feasible binding orientations, which were then ranked according to two primary metrics: the docking score (with more negative values reflecting stronger predicted affinity) and the confidence score (values greater than 0.7 indicating a high probability of genuine interaction). Post-docking, the top poses were evaluated and rendered in Surface representation.

Formation of the protein-nucleic acid complex relies on non-covalent contacts, chiefly hydrophobic interactions, hydrogen bonds, and electrostatic attractions. The binding interface was thoroughly examined using the PLIP platform, which offers a systematic and detailed characterization of these molecular interactions [30]. Additional structural insights were obtained through PyMOL visualization. PLIP is a specialized tool for detecting non-covalent protein-ligand interactions. In addition to assessing factors such as molecular size, shape complementarity, residue surface matching, and interface preferences, it performs atomic-level analysis of contacts including hydrophobic interactions, hydrogen bonds, water-mediated bridges, salt bridges, π-stacking, cation-π interactions, and halogen bonds. Detection is based on spatial distances and geometric criteria, with hydrophobic interactions assigned to all qualifying atom pairs located within 4.0 Å.

*RNA immunoprecipitation*

RNA immunoprecipitation (RIP) experiments were conducted with a commercial RIP Kit (Genseed, China). NSCLC cell lines (A549 and HCC2279) were collected and processed according to the established protocol [24].

*Transcriptome analysis*

NSCLC cells (A549 and HCC2279, seeded at $1 \times 10^5$ cells/well) were plated in 12-well plates and allowed to adhere for 24 h. Cells were then assigned to four experimental conditions: A549 siMYH9 (A-siMYH9), A549 control (A-siNC), HCC2279 siMYH9 (H-siMYH9), and HCC2279 control (H-siNC). Following the respective treatments, cultures were grown to full confluence. Monolayers were washed with PBS, after which 1 mL TRIzol reagent was added and the cells were lysed by repeated pipetting to ensure complete disruption. The lysates were transferred to tubes containing RNase-free deoxyribonuclease I. Total RNA was isolated from each group and stored at −80°C.

Reference-guided transcriptome sequencing was subsequently outsourced to Hangzhou LC Bio Technology CO., Ltd. RNA libraries were constructed using the Illumina TruSeqTM RNA sample preparation kit. Sequencing was performed on the Illumina PE150 platform, with downstream data processing conducted via NovoMagic. Differential expression analysis (DEGs) was performed between the A-siMYH9 versus A-siNC groups and the H-siMYH9 versus H-siNC groups using DESeq2, followed by functional annotation of the resulting DEGs. Genes were considered significantly differentially expressed if they satisfied padj ≤ 0.05 and |log2FC| ≥ 1.

Following identification of differentially expressed genes, functional enrichment analysis was carried out to uncover the principal signaling pathways and regulatory networks associated with the observed phenotypic changes. Gene annotation sets were assembled from resources such as the GO and KEGG databases. ClusterProfiler was then used to perform GO enrichment and KEGG pathway analyses on the DEG lists. GO classification organized genes into the categories of Biological Process (BP), Cellular Component (CC), and Molecular Function (MF). KEGG analysis identified statistically overrepresented signaling pathways. Pathways with padj < 0.05 were regarded as significantly enriched. Comparative analysis across the A549 and HCC2279 cell lines revealed a set of 190 common differentially expressed genes, which were visualized in a Venn diagram. These overlapping genes were further investigated through KEGG pathway and GO functional enrichment to determine their biological roles.

*Single-cell RNA sequencing*

Fresh xenograft tumor tissues were collected from nude mice belonging to the piR-hsa-164586 knockdown group and the corresponding control group. Single-cell RNA sequencing (scRNA-seq) was employed to investigate the expression profile of piR-hsa-164586 and the associated cellular alterations at single-cell resolution. Tissue samples were kept in storage solution at 2–8°C, transported on dry ice, and prepared into single-cell 3′ gene expression libraries using the 10× Genomics Chromium Single Cell 3′ Reagent Kit. Following preparation of a single-cell suspension, cells were captured and sequenced on the Illumina NovaSeq 6000 platform (Hangzhou LC Bio Technology CO., Ltd, China) at a minimum depth of 20,000 reads per cell.

Initial data processing of the scRNA-seq reads involved demultiplexing and conversion to FASTQ files with Illumina's bcl2fastq software (v2.20). Alignment, barcode assignment, and gene quantification were performed through the Cell Ranger pipeline (v6.1.1). Reads were mapped to the Ensembl GRCh38/GRCm38 reference genome. Processed outputs from Cell Ranger were loaded into Seurat (version 3.1.1) for further examination. Rigorous quality filtering removed low-quality cells according to the following thresholds: fewer than three genes detected, total gene count below 500, or mitochondrial gene content exceeding 25%. The filtered high-quality cells then proceeded to multiple downstream analyses, such as clustering, visualization and annotation, pseudotime trajectory modeling, intercellular communication inference, CytoTRACE scoring, regulon activity assessment, and functional enrichment.

The data were separated into human A549 tumor cell-derived populations and murine tumor microenvironment populations. In the human tumor cell compartment, cell clustering and subsequent sub-clustering were achieved with the FindClusters function in Seurat (version 4.1.1) at an appropriate resolution, combined with UMAP dimensionality reduction (resolution set at 0.2 using the first 20 dimensions). Differential expression testing across clusters relied mainly on the bimod algorithm, with statistical significance determined by $p < 0.01$ and $|\log2FC| \geq 0.26$. Cell proportion distributions within clusters were statistically assessed. CytoTRACE was subsequently applied to assign a potency score to each cell (ranging from 0 for differentiated cells to 1 for pluripotent cells). UMAP plots were generated via the plotData function to display potency scores, developmental ordering, and phenotypic labels. Intercellular communication networks were inferred using CellChat, an R package specialized for scRNA-seq-based ligand-receptor analysis. Communication events were classified as significant when the associated ligand-receptor p-value fell below 0.05. PySCENIC analysis was run with default settings (n = 50), incorporating the RcisTarget database and GRNboost (pySCENIC version 0.1.1.2). Identified regulatory networks were treated as regulons, enabling comparison of transcription factor activity across distinct cell types. Differential gene expression was considered significant at FDR < 0.05 and |log2FoldChange| > 0.26. Functional interpretation of DEGs was conducted via ClusterProfiler in R for both KEGG pathway and GO term enrichment. Significantly enriched pathways ($p < 0.05$) and GO terms ($p < 0.05$) were identified by comparing DEG lists against the respective databases. Results were visualized using bar or bubble plots in R.

For the murine tumor microenvironment dataset, processed cells underwent clustering, visualization, and annotation [31]. Clustering and sub-clustering were performed with Seurat's FindClusters function at resolution 0.2, utilizing the first 20 principal components. Inter-cluster differential expression was evaluated using the bimod test, with significance set at $p < 0.01$ and $|\log2FC| \geq 0.26$. Sample composition within each cluster was displayed in bar plots. Trajectory inference for epithelial, mesenchymal, and hybrid mesenchymal cells was carried out with Monocle (version 2.22.0). The differentialGeneTest function identified DEGs, and cells were arranged along pseudotime trajectories according to their expression profiles to reconstruct differentiation routes. Genes expressed in a minimum of 20 cells were assessed for their contribution to cell fate determination. Cell-to-cell

signaling was predicted using CellPhoneDB (version 3, www.cellphonedb.org). Significant interactions were defined by ligand-receptor p-values below 0.05. The seven clusters were re-evaluated according to EMT marker expression, including purely epithelial markers (Esrp1, Cdh1), mixed mesenchymal markers (Prrx1, Snai1, Zeb1, Zeb2, Pdgfra, Col3a1), and purely mesenchymal markers (Cdh2, Vim). Sample proportions in these clusters were illustrated with bar charts. Genes were ranked by average log2FC expression in the target population versus others, together with adjusted p-values; upregulated candidates were used to generate volcano plots. The identified DEGs then underwent KEGG and GO enrichment analysis.

*Human protein atlas database*

Data from the Human Protein Atlas (HPA) database (https://www.proteinatlas.org/) were examined to compare immunohistochemical staining patterns and confirm differences in target protein abundance between normal and cancerous tissues. Images were retrieved from the "Tissue" section for normal samples and the "Pathology" section for tumor samples. Normal lung tissue was used as the reference in the "Tissue" section, and LUAD samples were selected in the "Pathology" section. Expression of the interacting protein was compared between these groups, with differences considered statistically significant at $p < 0.05$.

*KM survival analysis*

RNA-seq profiles and matched clinical information for LUAD patients were sourced from The Cancer Genome Atlas (TCGA) database. Kaplan-Meier survival curves were generated in R using the survival package. Patients were stratified into high- and low-expression groups based on an optimal cutoff value of 7.7490. Analysis revealed a statistically significant difference in overall survival between the groups ($p < 0.05$).

*Pathway scores*

LUAD RNA sequencing data along with corresponding clinical variables were acquired from The TCGA database. A collection of EMT-related marker genes was compiled and evaluated for correlation with MYH9 expression levels via the GSVA package in R. Spearman's rank correlation analysis was applied to examine the relationship between gene expression and pathway activity scores, resulting in a p-value of $1.51 \times 10{-}10$. All statistical procedures were executed in R version 4.0.3, considering $p < 0.05$ as the threshold for significance.

*Statistical analysis*

All statistical evaluations were conducted with GraphPad Prism v8.0 (GraphPad Software) and SPSS v22.0 (IBM). Experiments were repeated in triplicate, and results were deemed significant at $p < 0.05$. Normality of data distribution was tested using the Kolmogorov–Smirnov test. Two-tailed Student's t-test was used for normally distributed continuous variables, while the Mann–Whitney U test was applied for non-parametric data. Multi-group comparisons were performed using one-way ANOVA for parametric data or the Kruskal–Wallis test for non-parametric distributions. Image quantification and processing were completed with ImageJ software (version 1.8.0.112).

**Results and Discussion**

*piR-hsa-164586 is overexpressed in NSCLC and is localized in both the nucleus and the cytoplasm*

A preceding study **(Figure 1a)** utilized high-throughput sequencing together with reverse transcription quantitative real-time polymerase chain reaction (RT-qPCR) to establish the increased abundance of extracellular vesicle-derived piRNAs in tumor samples from NSCLC patients [23]. The current research advanced this line of inquiry by examining the specific impact of piR-hsa-164586 on the migratory and invasive properties of NSCLC cells, thereby facilitating progress toward clinical molecular drug development aimed at this piRNA. Quantitative RT-qPCR measurements, in agreement with sequencing data, indicated significantly elevated expression of piR-hsa-164586 in NSCLC cell lines (A549 and HCC2279) relative to normal bronchial epithelial cells (BEAS-2B) **(Figure 1b)**, underscoring its relevance to NSCLC pathogenesis. Considering that methylation at the 3′ end of piRNAs confers protection against degradation and augments transcript stability [32], the 3′ methylation profile of piR-hsa-164586 was assessed via reverse transcription performed at low deoxyribonucleoside triphosphate concentrations followed by PCR amplification (RTL-P) **(Figures 1c and 1d)**. The outcomes verified the presence of this hallmark 3′ methylation modification characteristic of noncoding RNAs. RNA fluorescence in situ

hybridization (RNA-FISH) further localized piR-hsa-164586 to both nuclear and cytoplasmic compartments in NSCLC cells (A549 and HCC2279) **(Figure 1e)**. Taken together, these observations characterize the dysregulated expression and intracellular distribution of piR-hsa-164586, laying a solid foundation for deeper mechanistic studies of its contributions to NSCLC progression.

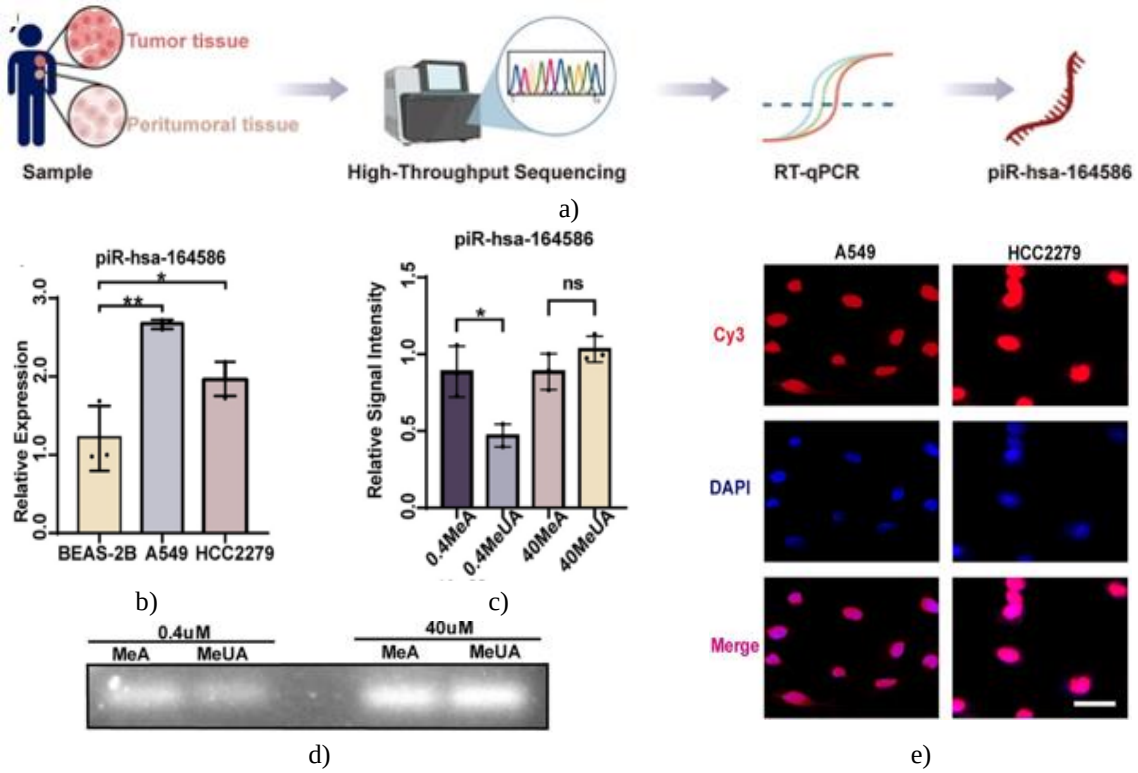


**Figure 1.** piR-hsa-164586 displays marked overexpression in NSCLC and resides in both nuclear and cytoplasmic compartments.

(a) Schematic diagram of piRNA screening and validation. (b) Real-time quantitative PCR analysis of piR-hsa-164586 in BEAS-2B cells and NSCLC cells (A549 and HCC2279). (c) Quantitative analysis of the data in (D). (d) Gel electrophoresis analysis of RTL-P. (e) PiR-hsa-164586 fluorescence in situ hybridization in A549 and HCC2279 cells (scale bar, 25 μm). Means ± standard deviations of three separate experiments are used for presentation of results *$p < 0.05$; **$p < 0.01$; NSCLC, non-small cell lung cancer; ns, not significant.

*piR-hsa-164586 stimulates NSCLC migration and invasion while suppressing apoptosis in vitro*

Functional validation of piR-hsa-164586's role in NSCLC was achieved through application of agomirs for overexpression and antagomirs for knockdown. Stable cell lines were successfully engineered in both A549 and HCC2279 backgrounds, encompassing the overexpression (OE), knockdown (KD), and normal control (NC) groups. Successful modulation was confirmed via RT-qPCR assessment of transfection efficiency **(Figure 2a)**. Data obtained from EdU incorporation and CCK-8 viability assays established a clear positive relationship between piR-hsa-164586 abundance and the proliferative activity as well as overall survival of NSCLC cells **(Figures 2b–2e)**. Wound healing and transwell chamber experiments further illustrated that heightened piR-hsa-164586 expression markedly enhanced cellular motility and invasiveness, whereas its depletion significantly attenuated these malignant traits **(Figures 2f–2h, 2j and 2l)**. Complementary flow cytometry experiments showed that piR-hsa-164586 upregulation effectively restrained apoptosis, while its reduction promoted programmed cell death (**Figures 2i and 2l)**. These collective findings firmly establish the critical contribution of this piRNA to the proliferative, migratory, and invasive properties of NSCLC cells.

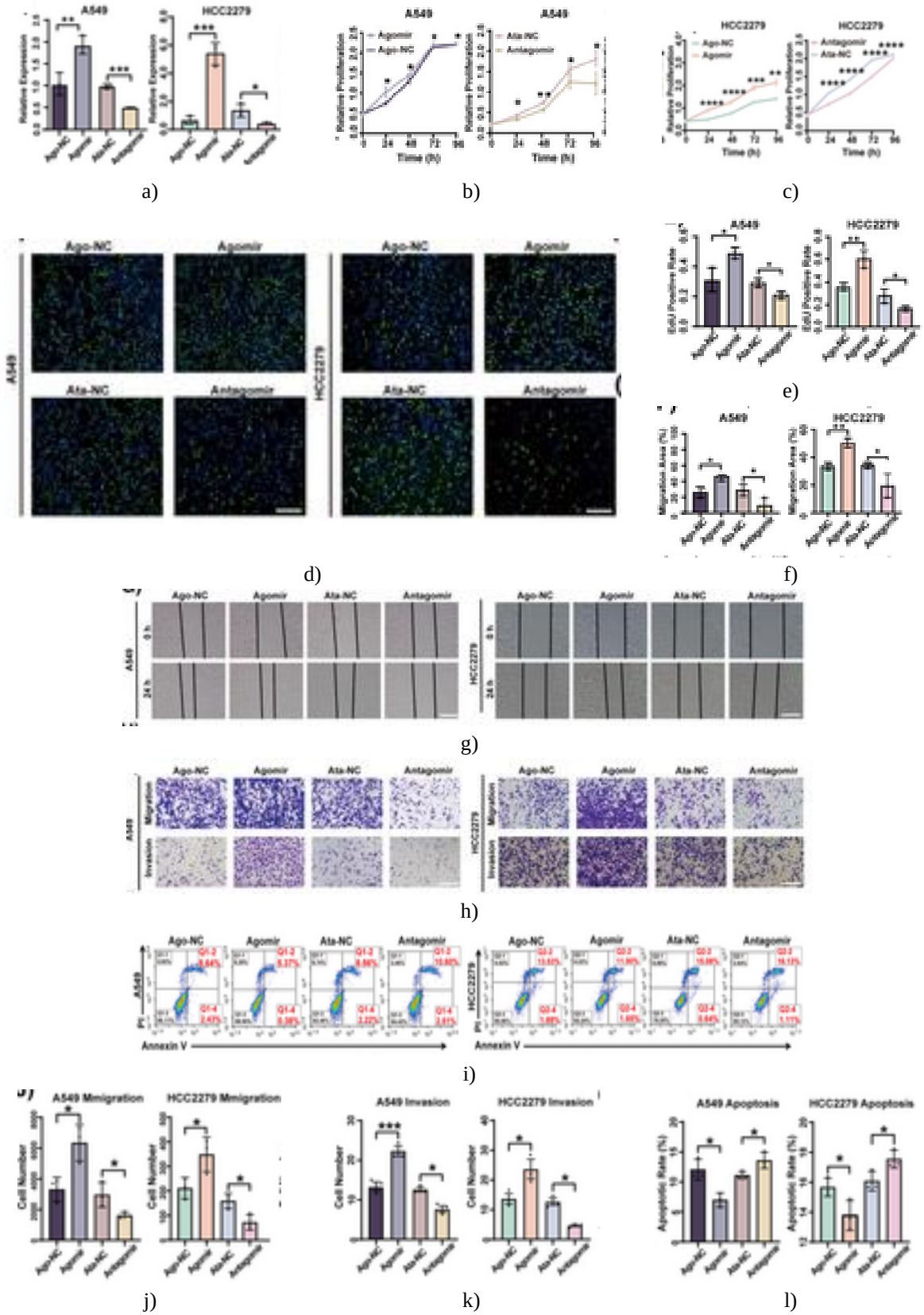


**Figure 2.** Effects of piR-hsa-164586 on NSCLC cell proliferation, migration, and apoptosis. (a) Relative quantification of real-time quantitative PCR data for piR-hsa-164586 after A549 and HCC2279 cells were treated with the agomir or antagomir. (b) CCK-8 assay of A549 cells in the agomir group and the antagomir group. (c) CCK-8 assay of HCC2279 cells in the agomir group and the antagomir group. (d) EdU assay of A549 and HCC2279 cells in the agomir group and the antagomir group (scale bar, 200 μm). (e) Quantitative analysis of the EdU assay results for A549 cells and HCC2279 cells. (f) Quantitative analysis of

the ability of A549 cells and HCC2279 cells to heal wounds. (g) Wound healing assays were conducted on A549 cells and HCC2279 cells treated with either the agomir or antagomir. Scale bar: 100 μm. (h) Transwell assays were conducted on A549 cells and HCC2279 cells treated with either agomir or antagomir (scale bar, 100 μm). (i) Flow cytometry analysis of A549 cells and HCC2279 cells treated with either agomir or antagomir. (j) Quantitative analysis of A549 and HCC2279 transwell migration assays. (k) Quantitative analysis of transwell invasion assays for A549 cells and HCC2279 cells. (l) Quantitative flow cytometric analysis of apoptotic A549 cells (red) and HCC2279 cells. Ago-NC, Agomir control; Ata-NC, Antagomir control; NSCLC, non-small cell lung cancer. The means ± standard deviations of three separate experiments are used to show the findings. *$p < 0.05$; **$p < 0.01$; ***$p < 0.001$; ****$p < 0.0001$.

*In vivo experiments confirmed the effect of piR-hsa-164586 on promoting tumor growth and metastasis and promoting angiogenesis*

In the xenograft model system, A549 cells modified for varying piR-hsa-164586 expression were introduced subcutaneously into immunodeficient nude mice to create an orthotopic NSCLC tumor model **(Figure 3a)**. Tumors arising from piR-hsa-164586-overexpressing cells displayed substantially greater size relative to controls, while those with reduced expression were notably smaller **(Figure 3b)**, highlighting a direct link between piR-hsa-164586 levels and tumor growth kinetics (TGR) [33]. Measurements of tumor volume and weight further corroborated this regulatory influence **(Figures 3c and 3d)**. Immunofluorescence detection of Ki67 demonstrated strong positive correlation with piR-hsa-164586 status, confirming enhanced proliferative activity **(Figures 3e and 3h)**. IHC staining revealed pronounced increases in α-SMA and CD31 protein levels within overexpressing tumors **(Figures 3f, 3g, 3i and 3j)**, supporting roles in metastatic facilitation and neovascularization, respectively. H&E histological examination showed denser nuclear staining in the overexpression group, indicative of accelerated cell division **(Figure 3k)**. These in vivo observations collectively substantiate piR-hsa-164586's capacity to drive tumor expansion, metastatic progression, and angiogenic processes in NSCLC.

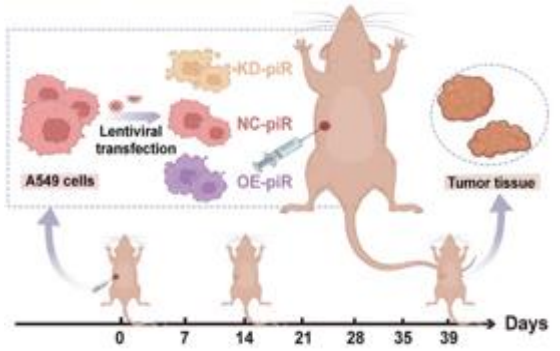


a)

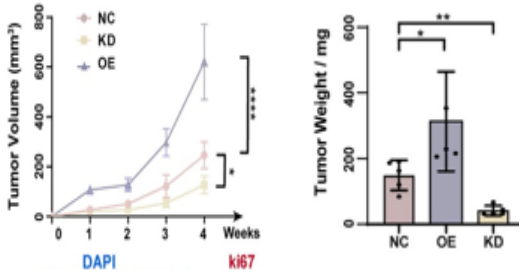


b) c)

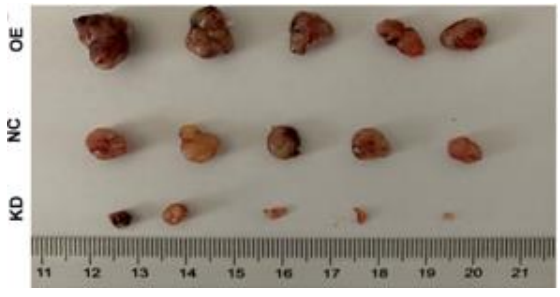


d)

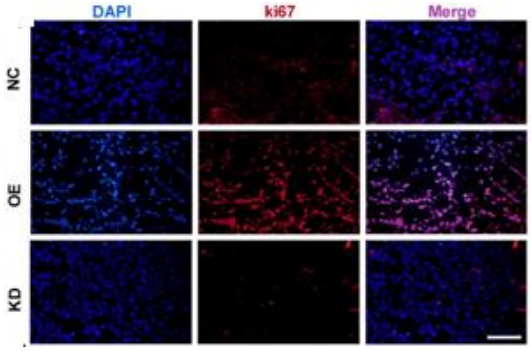


e)

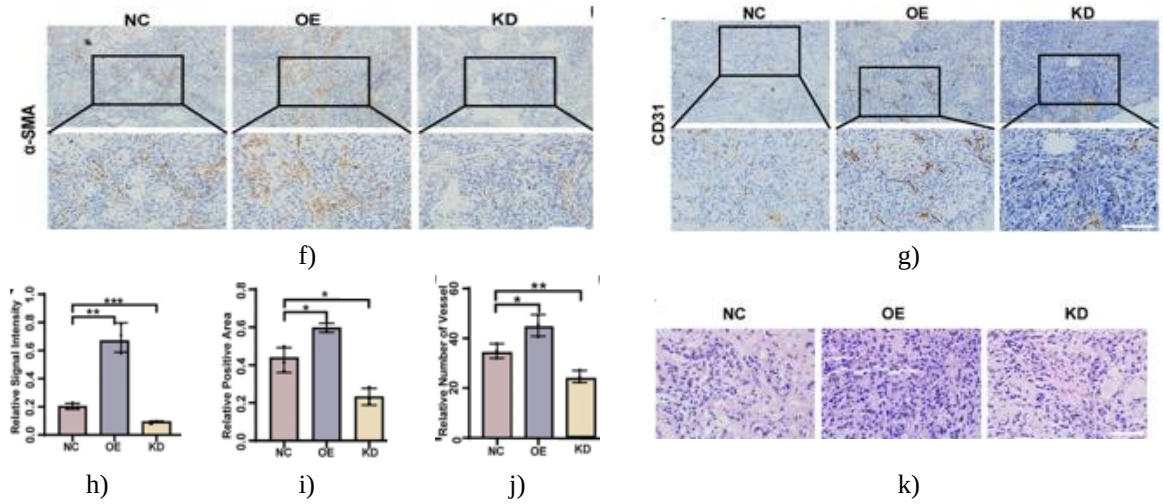


**Figure 3.** The regulatory effect of piR-hsa-164586 on A549 tumor was verified in vivo. (a) Schematic illustration of the subcutaneous A549 tumor-bearing process in BALB/c nude mice. (b) Curves representing the tumor growth volume over 1–4 weeks. (c) Tumors dissected from nude mice in each group. (d) tumor weights of the nude mice in each group. (e) Representative IF images of Ki67 staining in each group (scale bar, 50 μm). (f) Representative IHC images of α-SMA staining in each group (scale bar: 200 μm; enlarged view: 100 μm). (g) Representative IHC images of CD31 staining in each group (scale bar: 200 μm; enlarged view: 100 μm). (h) Quantitative analysis results of (e). (i) Quantitative analysis results of (f). (j) Quantitative results of (g). (k) HE staining of A549 tumors (scale bar, 50 μm). The results are expressed as the means ± SDs. *$p < 0.05$; **$p < 0.01$; ***$p < 0.001$; ns, not significant.

*scRNA-seq confirmed that piR-hsa-164586 affects tumor progression through the PI3K-AKT pathway*

To delineate the downstream pathways influenced by piR-hsa-164586 in NSCLC, scRNA-seq profiling was conducted **(Figure 4a)**. Following establishment of cell line-derived xenografts using A549 LUAD_EC cells in nude mice, clustering analysis resolved seven distinct LUAD_EC subpopulations **(Figure 4b)**: Mesenchymal LUAD_EC 1, Mesenchymal LUAD_EC 2, Matrix LUAD_EC, Proliferation LUAD_EC, Autophagy LUAD_EC, Adhesion LUAD_EC, and Pro-inflammatory LUAD_EC **(Figure 4c)**. Mesenchymal LUAD_EC 1 emerged as the dominant cluster, comprising 61.25% of the tumor cell population **(Figure 4d)**. Application of CytoTRACE for trajectory inference revealed that Proliferation LUAD_EC cells occupy an earlier, less differentiated state, whereas Mesenchymal LUAD_EC 1 and 2 represent later, more differentiated stages suggestive of EMT dynamics **(Figures 4e and 4f)**. The emergence of mesenchymal traits at advanced differentiation stages aligns with increased metastatic competence [34, 35], a hallmark feature in LUAD pathobiology.

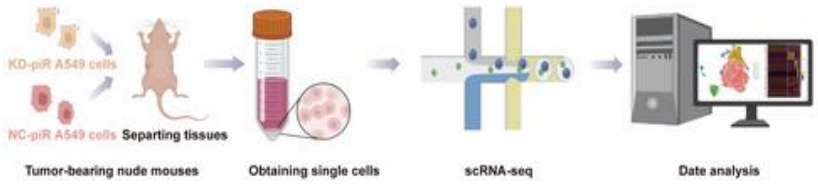


a)

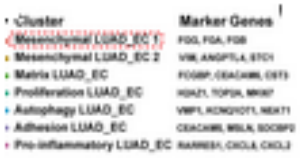


c)

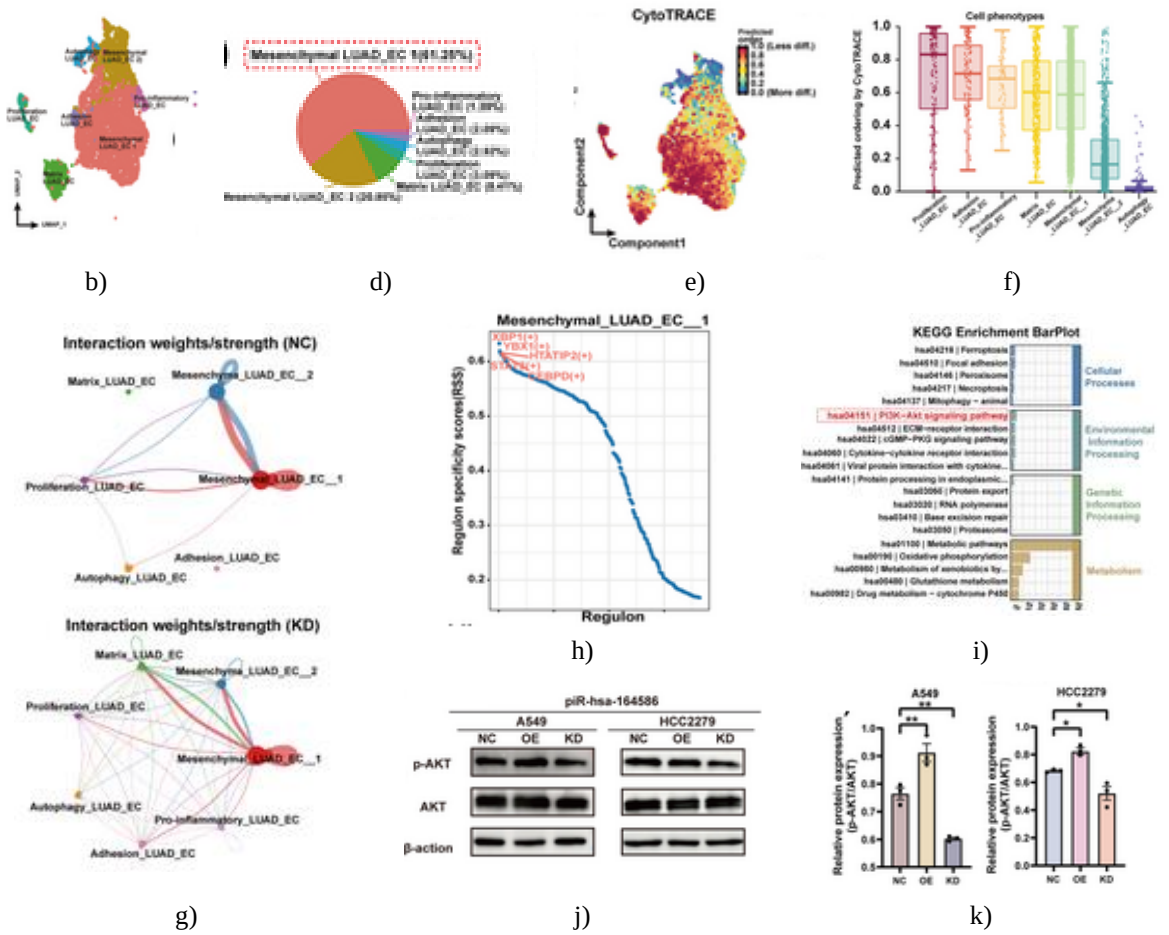


**Figure 4.** scRNA-seq of non-small cell lung cancer cells in nude mice.

(a) The workflow of scRNA-seq between the KD group and the negative control group of A549 cells in nude mice. (b) UMAP visualization of cellular subsets of tumor cells, including those in the piR-hsa-164586 control group and the piR-hsa-164586 knockdown group. (c) Characteristic genes associated with each cell cluster. (d) Cellular proportions of the tumor cell subsets. (e) CytoTRACE-predicted order distribution in tumor cells. The color gradient represents cell stemness, with different tones corresponding to high or low stemness. (f) The predicted ordering of cell differentiation trajectories by CytoTRACE. (g) Analysis of intercellular interaction weights/strength. (h) Ranking of regulons in Mesenchymal LUAD_EC 1 based on RSS. (i) Kyoto encyclopedia of genes and genomes hierarchical bar chart for the characteristic genes of Mesenchymal LUAD_EC 1. (j) Western blot analysis of p-AKT and AKT in A549 and HCC2279 cells subjected to different treatments. (k) Quantitative analysis of Western blot. Means ± standard deviations of three separate experiments are used for presentation of results. LUAD_EC, lung adenocarcinoma epithelial cell; NSCLC, non-small cell lung cancer; scRNA-seq, single-cell RNA sequencing. *$p < 0.05$; **$p < 0.01$.

Intercellular communication patterns were substantially more robust in the NC group than in the KD group, primarily involving interactions among Proliferation LUAD_EC, Mesenchymal LUAD_EC 1, and Mesenchymal LUAD_EC 2 subsets **(Figure 4g)**. Integrating subpopulation abundance, differentiation trajectories, and communication intensity pointed to Mesenchymal LUAD_EC 1 as a central driver in NSCLC advancement. Comparative transcriptomic analysis showed that this subpopulation is enriched for drug-resistance signatures rather than conventional cancer stem cell markers. Key transcription factors including XBP1(+), YBX1(+), HTAT1P2(+), STAT3(+), and CEBPD(+) were implicated in facilitating the phenotypic shift toward Mesenchymal LUAD_EC 2 **(Figure 4h)**. KEGG pathway analysis of the most differentially expressed genes prominently featured the PI3K-AKT cascade, ECM-receptor interactions, and oxidative phosphorylation **(Figure 4i)**. Consistent with these transcriptomic insights, western blotting confirmed elevated p-AKT/AKT ratios upon piR-hsa-164586 overexpression and reduced ratios following knockdown in both A549 and HCC2279 lines,

indicating that activation of the PI3K-AKT pathway represents a major mechanism underlying piR-hsa-164586-mediated promotion of tumor metastasis **(Figures 4j and 4k)**.

*scRNA-seq analysis demonstrated that piR-hsa-164586 potentially regulates the NSCLC microenvironment via EMT promotion*

Earlier research using scRNA-seq along with complementary experimental methods established that piR-hsa-164586 can increase phosphorylation of proteins in the PI3K-AKT signaling pathway, thereby driving NSCLC advancement. In this work, scRNA-seq was conducted on NSCLC tissues prior to and following piR-hsa-164586 knockdown to determine whether this piRNA modifies the tumor microenvironment **(Figure 5a)**. Seven predominant cell populations were recognized—B cells, endothelial cells (ECs), granulocytes, macrophages, mesenchymal cells, natural killer (NK) cells, and smooth muscle cells (SMCs)—based on their distinctive marker expression **(Figure 5b)**. Marked shifts were observed in the abundances of ECs and mesenchymal cells when comparing the piR-hsa-164586 knockdown (KD) group with the negative control (NC) group. Specifically, mesenchymal cells declined while ECs rose within the tumor tissues after knockdown **(Figure 5c)**. Additionally, lower piR-hsa-164586 levels correlated with reductions in B cells and granulocytes, accompanied by increases in macrophages, NK cells, and SMCs.

Evaluation of intercellular communication networks **(Figures 5d and 5e)** highlighted interactions between ECs and mesenchymal cells particularly in the KD group. These patterns indicate that depleting piR-hsa-164586 could hinder the conversion of ECs into mesenchymal-like cells. To explore EMT alterations more closely, ECs and mesenchymal subpopulations underwent further reclustering, resulting in 12 separate clusters. Bubble plots displayed the expression profiles of key EMT markers, such as epithelial indicators (Esrp1 and Cdh1), hybrid mesenchymal indicators (Prrx1, Snai1, Zeb1, Zeb2, Pdgfra, and Col3a1), and mesenchymal indicators (Cdh2 and Vim) [34]. Cluster 8 (Esrp1+/Cdh1+) represented the epithelial category, Cluster 4 (Cdh2+/Vim+) the mesenchymal category, and the other clusters were grouped as hybrid mesenchymal populations. Volcano plots identified the top five differentially expressed genes (DEGs) per cluster. Enrichment analysis of these DEGs pointed to involvement in extracellular matrix (ECM) production, immune responses, cytoskeletal remodeling, cell junctions and adhesion, cell cycle control, and cell division—all processes tightly connected to EMT. Using these characteristics, the 12 clusters were merged into three primary groups: ECs, mesenchymal cells, and hybrid mesenchymal cells **(Figure 5f)**. Bubble plots further visualized EMT marker expression across these groups **(Figure 5g)**. Pseudotime trajectory analysis captured the progressive EMT process. The mesenchymal population on the right of the trajectory corresponded to an intrinsic mesenchymal subset, while the left population appeared to arise from hybrid mesenchymal cells advancing to a mesenchymal phenotype, pointing to a newly recognized mesenchymal subtype **(Figure 5h)**.

Immunofluorescence (IF) staining performed on tumor tissues from nude mice revealed that elevating piR-hsa-164586 decreased E-cadherin (Cdh1) and increased N-cadherin (Cdh2), confirming its role in driving EMT in NSCLC **(Figure 5i)**. Overall, these observations establish that piR-hsa-164586 serves a critical function in controlling EMT in NSCLC, likely supporting tumor growth and metastatic spread by altering cell behaviors and remodeling the surrounding tumor microenvironment.

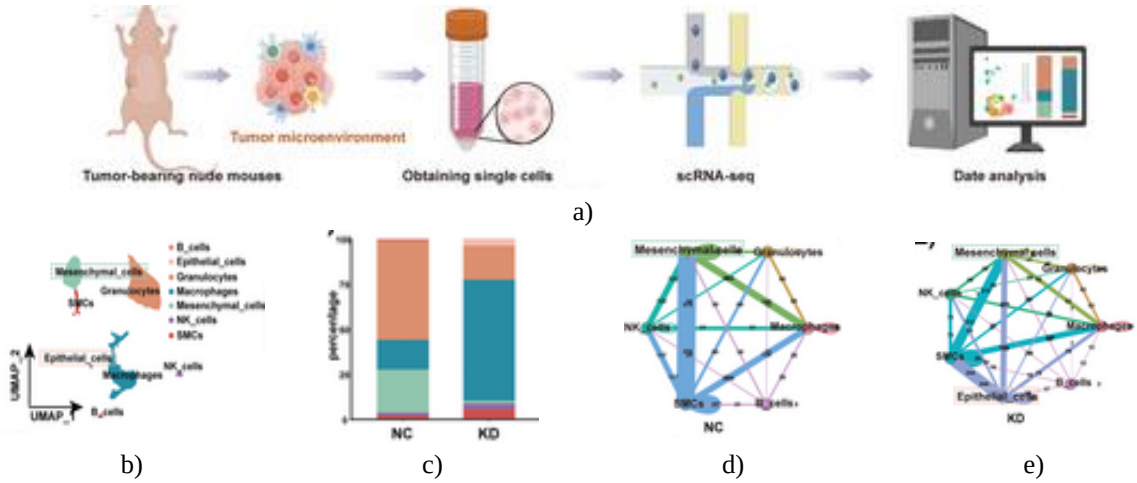

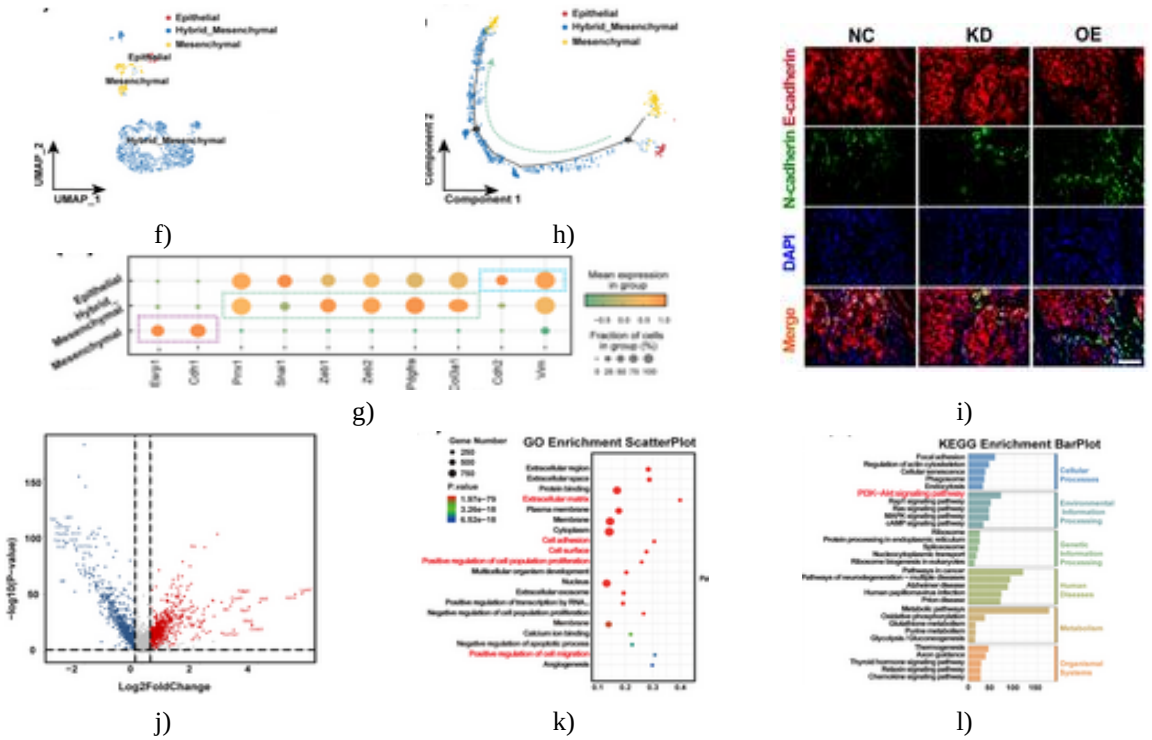


**Figure 5.** Mechanism of piR-hsa-164586-mediated EMT promotion in the non-small cell lung cancer microenvironment identified through scRNA-seq.

(a) Overview diagram of scRNA-seq applied to the tumor microenvironment in nude mice. (b) UMAP representation of the primary cellular clusters present in the tumor microenvironment of various samples. (c) Relative proportions of different cell types within the tumor microenvironment. (d) Cellular communication analysis in the piR-hsa-164586 control group. (e) Cellular communication analysis in the piR-hsa-164586-knockdown group. (f) UMAP visualization of reclustered EMT subpopulations (epithelial cells, hybrid mesenchymal cells, and mesenchymal cells). (g) Dot plot displaying marker genes for the EMT-reclustered populations. (h) Pseudotime trajectory of the EMT-reclustered cell populations. (i) Representative IF staining images demonstrating EMT (scale bar, 50 μm). (j) Identification of differentially expressed genes across groups. (k) Bar graph showing Gene Ontology enrichment of characteristic genes. (l) Hierarchical bar graph of Kyoto Encyclopedia of Genes and Genomes pathway enrichment for characteristic genes. EMT, epithelial-mesenchymal transition; scRNA-seq, single-cell RNA sequencing.

Differential gene expression analysis between the KD and NC groups was carried out **(Figure 5j)**. Gene Ontology (GO) enrichment highlighted strong associations with EMT-linked processes, including ECM adhesion, cell surface components, positive control of cell proliferation, and positive regulation of cell migration. KEGG pathway analysis showed clear enrichment in the PI3K-AKT cascade, matching previous results from tumor cells **(Figures 5k and 5l)**. These outcomes suggest that piR-hsa-164586 affects EMT development in the NSCLC microenvironment beyond its participation in the PI3K-AKT pathway.

*piR-hsa-164586 interacts with MYH9 to affect NSCLC cell progression*

Growing research shows that small non-coding RNAs (sncRNAs) advance cancer development by assembling complexes with proteins or additional RNA entities [36-39]. To examine whether piR-hsa-164586 modulates the PI3K-AKT pathway in cooperation with other proteins, mass spectrometry, RNA pull-down experiments, molecular docking simulations, and RNA immunoprecipitation (RIP) were integrated to detect protein partners of piR-hsa-164586 in NSCLC **(Figure 6a)**. Mass spectrometry data highlighted MYH9 with the greatest change, displaying a fold change of 727.1496805 and log2FC of 9.506088716 **(Figures 6b and 6c)**. MYH9 was therefore prioritized as the leading candidate for direct interaction with piR-hsa-164586. This protein is a cytoplasmic myosin crucial for diverse cellular activities and is alternatively termed non-muscle myosin heavy chain IIA (NMMHC-IIA) [40]. The present findings add to knowledge of MYH9's contribution to NSCLC advancement.

A multi-method strategy was then used to verify the piR-hsa-164586–MYH9 interaction. RNA pull-down assays employed biotinylated piR-hsa-164586 incubated with cytoplasmic lysates from A549 and HCC2279 cells. Western blotting verified the strong association between piR-hsa-164586 and MYH9 **(Figure 6d)**. Molecular docking using the HDOCKlite v1.1 server predicted the interaction model with the lowest binding energy, achieving a docking score of −515.91 and a confidence score of 0.9993, supporting a likely binding conformation **(Figure 6e)**. Surface visualization illustrated contact zones, while protein-ligand interaction profiler (PLIP) analysis detected 11 hydrogen bonds and 4 salt bridges. RIP assays independently confirmed direct binding of piR-hsa-164586 to MYH9 **(Figure 6f)**.

Western blot experiments indicated a positive relationship between piR-hsa-164586 expression and MYH9 protein levels **(Figures 6g–6i)**. Similar results appeared in IF staining for MYH9 **(Figures 6i and 6j)**. qRT-PCR analysis of MYH9 mRNA also showed a positive correlation with piR-hsa-164586. Together, these results point to piR-hsa-164586 promoting NSCLC initiation and progression through its physical interaction with MYH9.

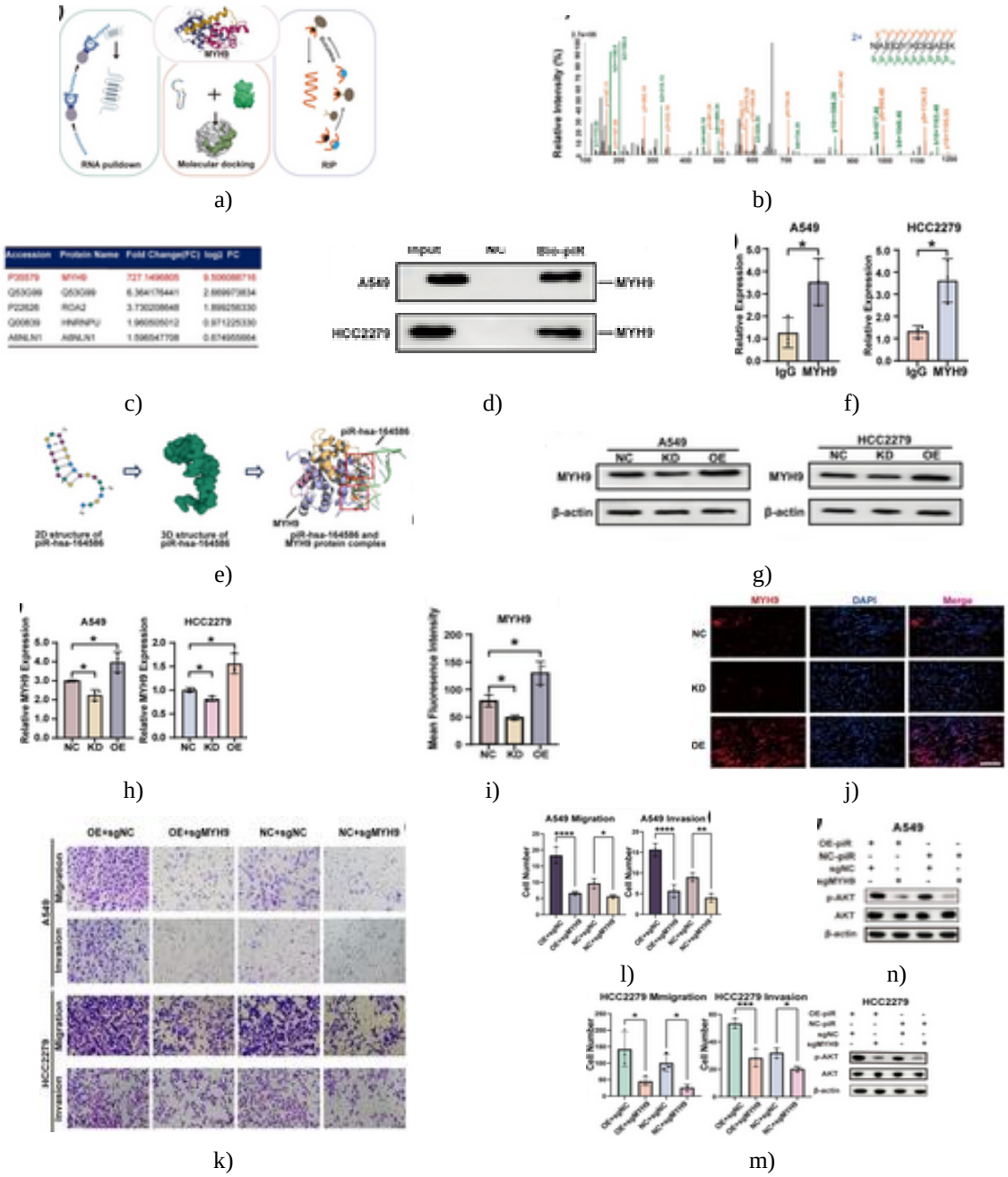


**Figure 6.** piR-hsa-164586 targets MYH9 and modulates cell migration and invasion.

(a) Schematic workflow for identifying MYH9 as an interaction partner of piR-hsa-164586. (b) MS spectra of representative MYH9 peptides. The peptide sequence analyzed was NAEQYKDQADK. (c) Quantitative

protein levels determined by MS. (d) RNA pull-down assay confirming interaction between MYH9 and biotinylated piR-hsa-164586 probes in A549 and HCC2279 cells via Western blot. (e) Molecular docking model of piR-hsa-164586 bound to MYH9. (f) RIP assay results showing MYH9 immunoprecipitation and associated RNA enrichment assessed by qRT-PCR in A549 and HCC2279 cells. (g) Western blot of MYH9 protein levels after piR-hsa-164586 overexpression or knockdown. (h) Quantitative analysis of data from (g). (i) Quantitative analysis of data from (j). (j) IF staining images of MYH9 under piR-hsa-164586 overexpression or knockdown conditions (scale bar, 50 μm). (k) Transwell migration and invasion assays in A549 and HCC2279 cells with various treatments (scale bar, 100 μm). (l, m) Quantitative results from (k). (n) Western blot analysis of MYH9 protein in A549 and HCC2279 cells under different treatments. Data are expressed as means ± standard deviations from three independent experiments. MS, mass spectrometry. *$p < 0.05$; **$p < 0.01$; ***$p < 0.001$; ****$p < 0.0001$.

To substantiate the functional relevance of the piR-hsa-164586–MYH9 interaction for NSCLC cell migration and invasion, a CRISPR/Cas9-based MYH9 knockout system was developed and validated by Western blot and qRT-PCR. Subsequent transwell assays showed that MYH9 deletion substantially impaired migration and invasion in A549 and HCC2279 cells. Overexpression of piR-hsa-164586 strongly enhanced these abilities and partially counteracted the suppression caused by MYH9 loss ($p < 0.05$), establishing MYH9 as a key downstream mediator **(Figures 6k–6m)**. Western blot rescue experiments further revealed that piR-hsa-164586 overexpression raised the P-AKT/AKT ratio, which was lowered by MYH9 knockout, with partial restoration upon piR-hsa-164586 re-expression **(Figure 6n)**.

Parallel experiments using siRNA-mediated MYH9 knockdown (employing siMYH9-homo-3074 with optimal efficiency) produced consistent outcomes. In summary, the evidence confirms that piR-hsa-164586 cooperates with MYH9 to drive NSCLC cell migration and invasion. These insights propose that interventions directed at the piR-hsa-164586–MYH9 interaction could offer valuable new therapeutic options for managing aggressive NSCLC.

*Transcriptomic profiling identified MYH9 as a driver of NSCLC advancement through PI3K-AKT signaling and EMT induction*

To define the exact molecular contributions of MYH9 to NSCLC tumorigenesis, researchers generated stable MYH9-silenced lines in both A549 and HCC2279 cells **(Figure 7a)**. Subsequent whole-transcriptome sequencing assessed broad gene expression shifts resulting from altered MYH9 abundance. This approach yielded 190 DEGs shared between the two cell lines **(Figure 7b)**. KEGG enrichment analysis indicated strong overrepresentation of the PI3K-AKT signaling cascade among these genes **(Figure 7c)**, corroborating earlier single-cell findings. GO term analysis similarly underscored enrichment for EMT (GO:0051607), a phenotype downstream of PI3K-AKT activity **(Figure 7d)** [41] Overall, the data support the notion that MYH9 promotes metastatic spread in NSCLC by influencing both the PI3K-AKT axis and EMT programs.

Examination of IHC images from the Human Protein Atlas (HPA) database showed markedly higher MYH9 protein abundance in NSCLC tumor specimens compared with non-malignant lung tissue, highlighting its potential clinical importance **(Figures 7e and 7f)**. Mining of TCGA RNA-seq datasets paired with patient metadata for LUAD cases **(Figure 7g)** revealed that tumors with high MYH9 expression exhibited elevated EMT scores, linking this protein to enhanced invasiveness and metastatic traits. Kaplan-Meier survival curves further demonstrated that increased MYH9 levels were significantly associated with reduced overall survival **(Figure 7h)**. Thus, integrative transcriptomic and clinicopathologic evidence positions MYH9 as a key mediator of NSCLC progression mediated by PI3K-AKT signaling and EMT.

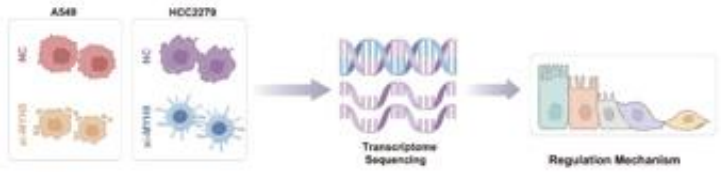


a)

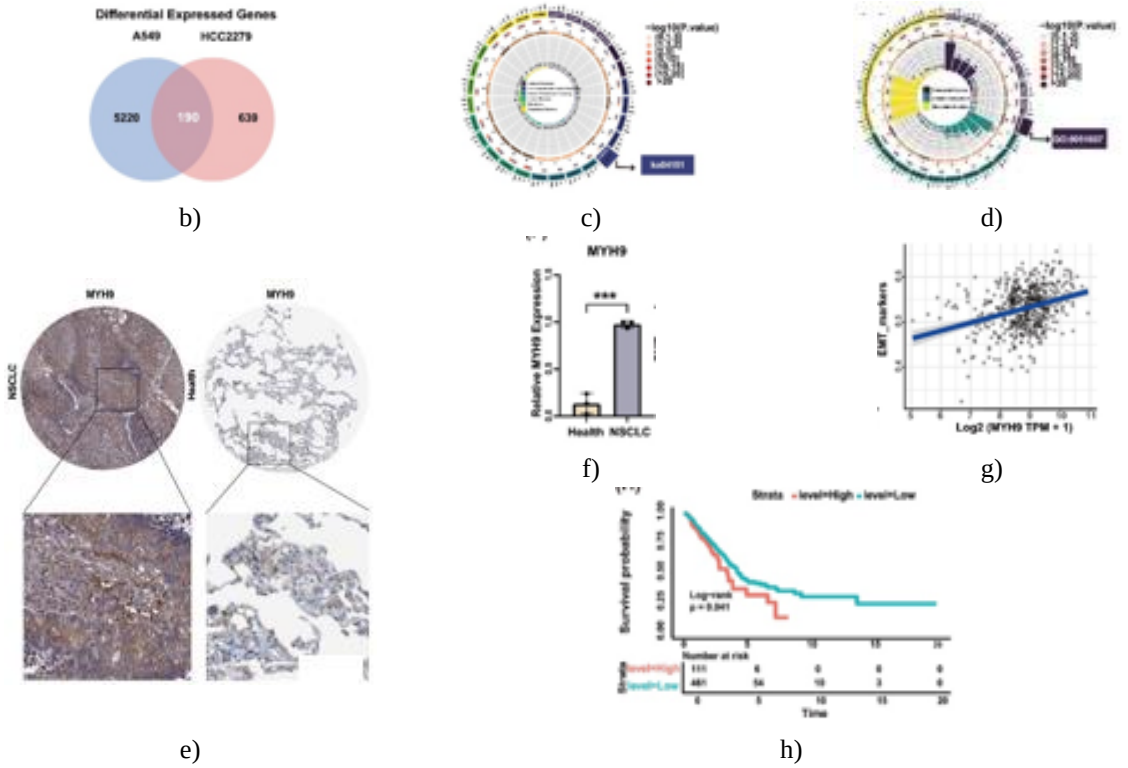


**Figure 7.** Transcriptome sequencing results from A549 and HCC2279 cells following experimental manipulations.

(a) Experimental workflow for transcriptome sequencing. (b) Venn diagram depicting shared differentially expressed genes identified in MYH9-knockdown A549 and HCC2279 cells. (c) Kyoto Encyclopedia of Genes and Genomes pathway enrichment for overlapping genes. (d) Gene Ontology enrichment for overlapping genes. (e) Immunohistochemical detection of MYH9 in non-small cell lung cancer specimens versus normal controls. (f) Quantitative evaluation of staining intensity from (e). (g) Association between MYH9 expression and EMT marker genes, $p < 0.05$. (h) Kaplan-Meier survival curves for lung adenocarcinoma patients stratified by MYH9 levels, $p < 0.05$. Data represent means ± standard deviations of three independent experiments. ***$p < 0.001$.

Metastatic dissemination constitutes the predominant cause of dismal outcomes in cancer [42], with dysregulated piRNA expression frequently implicated in heightened tumor cell invasiveness and metastatic capacity [43], While extensive literature documents piRNA functions across diverse malignancies, investigations specific to NSCLC remain comparatively scarce. Earlier work by the authors identified exosomal piR-hsa-164586 detectable in NSCLC tissue and serum as a promising diagnostic indicator; however, its therapeutic potential as a gene-targeting agent had not been examined. The current investigation represents the initial detailed characterization of piR-hsa-164586's contributions and mechanistic actions in driving tumor advancement **(Figure 8)**. These insights expand knowledge regarding piRNA participation in NSCLC metastasis and supply a conceptual framework for designing innovative gene- and protein-directed therapies.

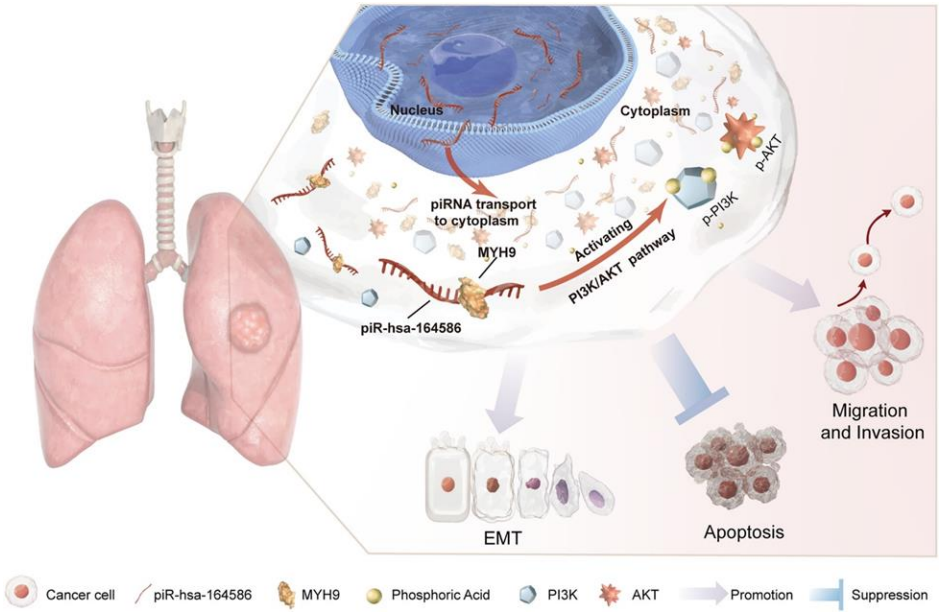


**Figure 8.** Schematic representation of the mechanism.

This illustration shows the mechanistic interplay between piR-hsa-164586, MYH9, the PI3K-AKT pathway, and EMT, highlighting the pivotal role of this axis in the regulation of NSCLC cell behavior. Specifically, by regulating the PI3K-AKT pathway and EMT, piR-hsa-164586 is involved in the development of NSCLC. In addition, piR-hsa-164586 combines with a non-PIWI protein (MYH9) downstream to disrupt the tumor microenvironment and promote the invasion and metastasis of NSCLC cells. EMT, epithelial-mesenchymal transition; NSCLC, non-small cell lung cancer.

Mechanistic control of tumor biology by piRNAs is intricate. Beyond canonical interactions with PIWI proteins, these molecules can affect oncogenic processes via associations with diverse protein partners and epigenetic modulators [36-38]. The present work provides original evidence that piR-hsa-164586 physically interacts with and controls the non-PIWI protein MYH9. Based on available knowledge, piRNAs are postulated to influence MYH9 stability by interfering with ubiquitination-dependent turnover. Proposed routes include: competition with other binding partners to shield MYH9 from E3 ubiquitin ligases, thereby decreasing its ubiquitination and degradation [44]; direct engagement with E3 ligases to prevent their docking onto MYH9 and suppress ubiquitination [45]; or modulation of transcription factors such as c-Jun to boost MYH9 gene transcription and protein synthesis, indirectly limiting ubiquitin-mediated breakdown [46].

Aberrant MYH9 levels correlate with aggressive behavior in numerous tumor types, where the protein governs critical processes such as cell motility, invasion, adhesion, cytokinesis, polarity establishment, cytoskeletal integrity, and intracellular signaling [26, 47, 48]. Acting in concert with piR-hsa-164586, MYH9 appears to synergistically accelerate tumor growth and dissemination. Consequently, therapeutic disruption of either component may yield improved clinical management of NSCLC and open new avenues for exploring non-PIWI-dependent piRNA activities.

A further notable contribution of this research lies in elucidating how piR-hsa-164586 reshapes the NSCLC tumor microenvironment. By combining single-cell transcriptomics with complementary molecular assays, the study showed that increased piR-hsa-164586 drives expansion of mesenchymal cell states within LUAD-associated endothelial populations, thereby intensifying EMT programs and facilitating metastatic dissemination. These discoveries illuminate the regulatory circuitry of piR-hsa-164586 and introduce an expanded viewpoint on dynamic microenvironmental remodeling in NSCLC.

scRNA-seq and transcriptomic profiling further established that piR-hsa-164586 and MYH9 contribute to NSCLC advancement by modulating the PI3K-AKT signaling cascade and EMT program. The PI3K-AKT pathway exhibits strong associations with unfavorable cancer outcomes and functions as a central driver of metastatic dissemination in various malignancies [49-52]. Moreover, activation of EMT strongly correlates with enhanced tumor cell capacity for invasion and colonization of distant sites [53]. Cells exhibiting hybrid epithelial-mesenchymal features display particularly potent metastatic potential [54]. Earlier investigations have documented piRNA-mediated control of these pathways in other tumor contexts. The present work not only

corroborates these observations but also provides the first detailed molecular delineation of how piR-hsa-164586 governs NSCLC metastasis, supported by comprehensive cellular and genomic evidence. These findings identify a novel therapeutic target and furnish a mechanistic foundation for improved NSCLC management.

While this investigation has examined piRNA functions in NSCLC, broader validation through larger cohorts is required to confirm the robustness and applicability of the results. Additional functional studies are necessary to solidify the main conclusions. Future efforts should prioritize detailed characterization of the molecular interface between piR-hsa-164586 and both MYH9 protein and mRNA. Furthermore, evaluating synergistic effects of piR-hsa-164586 or MYH9 inhibitors combined with standard treatments—including chemotherapy, radiotherapy, and immunotherapy—represents an important direction for advancing targeted molecular therapies in NSCLC.

## Conclusion

This study pioneered the combined application of scRNA-seq and transcriptome sequencing to investigate piRNA functions in NSCLC. It uncovered a previously unrecognized interaction between piR-hsa-164586 and the non-PIWI protein MYH9, together with their joint regulation of tumor progression via the PI3K-AKT pathway and EMT. These results offer fresh perspectives on tumor microenvironment remodeling during NSCLC development and highlight promising candidates for future clinical intervention.

**Acknowledgments:** None

**Conflict of Interest:** None

**Financial Support:** None

**Ethics Statement:** None

## References

1. International Agency for Research on Cancer. Saudi Med J. 2024;45:326.
2. He Y, Jiang X, Duan L, Xiong Q, Yuan Y, Liu P, et al. LncRNA PKMYT1AR promotes cancer stem cell maintenance in non-small cell lung cancer via activating Wnt signaling pathway. Mol Cancer. 2021;20(1):156.
3. Shimizu R, Kinoshita T, Sasaki N, Uematsu M, Sugita Y, Shima T, et al. Clinicopathological factors related to recurrence patterns of resected non-small cell lung cancer. J Clin Med. 2020;9(8):2473.
4. Feng H, Xu H, Shi X, Ding G, Yan C, Li L, et al. TP53 exon 5 mutation indicates poor progression-free survival for patients with stage IV NSCLC. Front Biosci. 2023;28(7):147.
5. Pang W, Gong L, Shi W, Zheng H, Ye M, Chen J, et al. Discov Oncol. 2024;15:67.
6. Malone ER, Oliva M, Sabatini PJB, Stockley TL, Siu LL. Molecular profiling for precision cancer therapies. Genome Med. 2020;12(1):8.
7. Xu L, Huang X, Lou Y, Xie W, Zhao H. Regulation of apoptosis, autophagy and ferroptosis by non-coding RNAs in metastatic non-small cell lung cancer. Exp Ther Med. 2022;23(5):352.
8. Cui X, Wang J, Guo Z, Li M, Li M, Liu S, et al. Emerging function and potential diagnostic value of circular RNAs in cancer. Mol Cancer. 2018;17(1):123.
9. Zhang Q, Zhu Y, Cao X, Tan W, Yu J, Lu Y, et al. The epigenetic regulatory mechanism of PIWI/piRNAs in human cancers. Mol Cancer. 2023;22(1):45.
10. Liu Y, Dou M, Song X, Dong Y, Liu S, Liu H, et al. The emerging role of the piRNA/piwi complex in cancer. Mol Cancer. 2019;18(1):123.
11. Ding L, Wang R, Xu W, Shen D, Cheng S, Wang H, et al. PIWI-interacting RNA 57125 restrains clear cell renal cell carcinoma metastasis by downregulating CCL3 expression. Cell Death Discov. 2021;7(1):333.
12. Xie Q, Li Z, Luo X, Wang D, Zhou Y, Zhao J, et al. piRNA-14633 promotes cervical cancer cell malignancy in a METTL14-dependent m6A RNA methylation manner. J Transl Med. 2022;20(1):51.
13. Li D, Luo Y, Gao Y, Yang Y, Wang Y, Xu Y, et al. piR-651 promotes tumor formation in non-small cell lung carcinoma through the upregulation of cyclin D1 and CDK4. Int J Mol Med. 2016;38(3):927.

14. Gainetdinov I, Colpan C, Cecchini K, Arif A, Jouravleva K, Albosta P, et al. Terminal modification, sequence, length, and PIWI-protein identity determine piRNA stability. Mol Cel. 2021;81(23):4826.
15. Wang K, Wang S, Zhang Y, Xie L, Song X, Song X. SNORD88C guided 2′-O-methylation of 28S rRNA regulates SCD1 translation to inhibit autophagy and promote growth and metastasis in non-small cell lung cancer. Cell Death Differ. 2023;30(2):341.
16. Dong J, Wang X, Cao C, Wen Y, Sakashita A, Chen S, et al. UHRF1 suppresses retrotransposons and cooperates with PRMT5 and PIWI proteins in male germ cells. Nat Commun. 2019;10(1):4705.
17. Chen S, Ben S, Xin J, Li S, Zheng R, Wang H, et al. The biogenesis and biological function of PIWI-interacting RNA in cancer. J Hematol Oncol. 2021;14(1):93.
18. Girard A, Sachidanandam R, Hannon GJ, Carmell MA. A germline-specific class of small RNAs binds mammalian Piwi proteins. Nature. 2006;442(7099):199.
19. Jia DD, Jiang H, Zhang YF, Qian LL. The regulatory function of piRNA/PIWI complex in cancer and other human diseases: The role of DNA methylation. Int J Biol Sci. 2022;18(8):3358.
20. Tan L, Mai D, Zhang B, Jiang X, Zhang J, Bai R, et al. PIWI-interacting RNA-36712 restrains breast cancer progression and chemoresistance by interaction with SEPW1 pseudogene SEPW1P RNA. Mol Cancer. 2019;18(1):9.
21. Xu Z, Liu M, Wang J, Liu K, Xu L, Fan D, et al. Single-cell RNA-sequencing analysis reveals MYH9 promotes renal cell carcinoma development and sunitinib resistance via AKT signaling pathway. Cell Death Discov. 2022;8(1):125.
22. Zhao B, Qi Z, Li Y, Wang C, Fu W, Chen YG. The non-muscle-myosin-II heavy chain Myh9 mediates colitis-induced epithelium injury by restricting Lgr5+ stem cells. Nat Commun. 2015;6(1):7166.
23. Li Y, Dong Y, Zhao S, Gao J, Hao X, Wang Z, et al. Serum-derived piR-hsa-164586 of extracellular vesicles as a novel biomarker for early diagnosis of non-small cell lung cancer. Front Oncol. 2022;12:850363.
24. Liu Y, Dong Y, He X, Gong A, Gao J, Hao X, et al. piR-hsa-211106 inhibits the progression of lung adenocarcinoma through pyruvate carboxylase and enhances chemotherapy sensitivity. Front Oncol. 2021;11:651915.
25. Chen J, Fan J, Chen Z, Zhang M, Peng H, Liu J, et al. Nonmuscle myosin heavy chain IIA facilitates SARS-CoV-2 infection in human pulmonary cells. Proc Natl Acad Sci USA. 2021;118(50):e2111011118.
26. Liu F, Peng L, XI J. Nan Fang Yi Ke Da Xue Xue Bao. 2023;43:527.
27. Mijit A, Wang X, Li Y, Xu H, Chen Y, Xue W. Mapping synthetic binding proteins epitopes on diverse protein targets by protein structure prediction and protein-protein docking. Comput Biol Med. 2023;163:107183.
28. Pecci A, Ma X, Savoia A, Adelstein RS. MYH9: Structure, functions and role of non-muscle myosin IIA in human disease. Gene. 2018;664:152.
29. Yan Y, Tao H, He J, Huang SY. The HDOCK server for integrated protein–protein docking. Nat Protoc. 2020;15(5):1829.
30. Adasme MF, Linnemann KL, Bolz SN, Kaiser F, Salentin S, Haupt V, et al. PLIP 2021: expanding the scope of the protein–ligand interaction profiler to DNA and RNA. Nucleic Acids Res. 2021;49(W1):W530.
31. Hou Y, Sun L, Lafleur MW, Huang L, Lambden C, Thakore PI, et al. Neuropeptide signalling orchestrates T cell differentiation. Nature. 2024;635(8038):444.
32. Izumi N, Shoji K, Suzuki Y, Katsuma S, Tomari Y. Zucchini consensus motifs determine the mechanism of pre-piRNA production. Nature. 2020;578(7794):311.
33. Nishino M, Hida T, Kravets S, Dahlberg SE, Lydon CA, Hatabu H, et al. Tumor volume dynamics and tumor growth rate in ALK-rearranged advanced non-small-cell lung cancer treated with crizotinib. Eur J Radiol Open. 2020;7:100210.
34. Pastushenko I, Brisebarre A, Sifrim A, Fioramonti M, Revenco T, Boumahdi S, et al. Identification of the tumour transition states occurring during EMT. Nature. 2018;556(7702):463.
35. Feng J, Hu S, Liu K, Sun G, Zhang Y. The role of MicroRNA in the regulation of tumor epithelial–mesenchymal transition. Cells. 2022;11(13):1981.
36. Liu H, Li D, Sun L, Qin H, Fan A, Meng L, et al. Interaction of lncRNA MIR100HG with hnRNPA2B1 facilitates m6A-dependent stabilization of TCF7L2 mRNA and colorectal cancer progression. Mol Cancer. 2022;21(1):74.

37. Sun Y, Tian Y, He J, Zhang G, Zhao R, Zhu W, et al. Linc01133 contributes to gastric cancer growth by enhancing YES1-dependent YAP1 nuclear translocation via sponging miR-145-5p. Cell Death Dis. 2022;13(1):51.
38. Xie J, Xing S, Shen BY, Chen HT, Sun B, Wang ZT, et al. PIWIL1 interacting RNA piR-017061 inhibits pancreatic cancer growth via regulating EFNA5. Hum Cell. 2021;34(2):550.
39. Ren X, Zhu H, Deng K, Ning X, Li L, Liu D, et al. Long noncoding RNA TPRG1-AS1 suppresses migration of vascular smooth muscle cells and attenuates atherogenesis via interacting with MYH9 protein. Arterioscler Thromb Vasc Biol. 2022;42(11):1378.
40. Li Y, Pan Y, Yang X, Wang Y, Liu B, Zhang Y, et al. Unveiling the enigmatic role of MYH9 in tumor biology: a comprehensive review. Cell Commun Signal. 2024;22(1):417.
41. Sun C, Tao Y, Gao Y, Xia Y, Liu Y, Wang G, et al. F-box protein 11 promotes the growth and metastasis of gastric cancer via PI3K/AKT pathway-mediated EMT. Biomed Pharmacother. 2018;98:416.
42. Xu WW, Huang ZH, Liao L, Zhang Q, Li J, Zheng C, et al. Direct targeting of CREB1 with imperatorin inhibits TGFβ2-ERK signaling to suppress esophageal cancer metastasis. Adv Sci. 2020;7(16):2000925.
43. Xu L, Ma W, Huo X, Luo J, Li R, Zhu X, et al. New insights into the function and mechanisms of piRNA PMLCPIR in promoting PM2. 5-induced lung cancer. J Adv Res. 2025;73:659.
44. Zhou J, Wu L, Li W, Xu X, Ju F, Yu S, et al. Long noncoding RNA LINC01485 promotes tumor growth and migration via inhibiting EGFR ubiquitination and activating EGFR/Akt signaling in gastric cancer. OncoTargets Ther. 2020;13:8413.
45. Li Q, Luo H, Dai FQ, Wang R, Fan X, Luo Y, et al. SAMD9 promotes postoperative recurrence of esophageal squamous cell carcinoma by stimulating MYH9-mediated GSK3β/β-catenin signaling. Adv Sci. 2023;10(11):2203573.
46. Que T, Zheng H, Zeng Y, Liu X, Qi G, La Q, et al. HMGA1 stimulates MYH9-dependent ubiquitination of GSK-3β via PI3K/Akt/c-Jun signaling to promote malignant progression and chemoresistance in gliomas. Cell Death Dis. 2021;12(12):1147.
47. Wang B, Qi X, Liu J, Zhou R, Lin C, Shangguan J, et al. MYH9 promotes growth and metastasis via activation of MAPK/AKT signaling in colorectal cancer. J Cancer. 2019;10(4):874.
48. Liu Q, Cheng C, Huang J, Yan W, Wen Y, Liu Z, et al. MYH9: A key protein involved in tumor progression and virus-related diseases. Biomed Pharmacother. 2024;171:116118.
49. Zhang R, Xu Y, Ekman N, Wu Z, Wu J, Alitalo K, et al. Etk/Bmx transactivates vascular endothelial growth factor 2 and recruits phosphatidylinositol 3-kinase to mediate the tumor necrosis factor-induced angiogenic pathway. J Biol Chem. 2003;278(51):51267.
50. Huang CC, Chiou CH, Liu SC, Hu S, Su C, Tsai C, et al. Melatonin attenuates TNF-α and IL-1β expression in synovial fibroblasts and diminishes cartilage degradation: Implications for the treatment of rheumatoid arthritis. J Pineal Res. 2019;66(3):e12560.
51. Kerbel RS. Tumor angiogenesis. N Engl J Med. 2008;358(19):2039.
52. He Y, Sun MM, Zhang GG, Yang J, Chen KS, Xu WW, et al. Targeting PI3K/Akt signal transduction for cancer therapy. Signal Transduct Target Ther. 2021;6(1):425.
53. Liang S, Guo H, Ma K, Li X, Wu D, Wang Y, et al. A PLCB1–PI3K–AKT signaling axis activates EMT to promote cholangiocarcinoma progression. Cancer Res. 2021;81(23):5889.
54. Udugampolage NS, Frolova S, Taurino J, Pini A, Martelli F, Voellenkle C. Coding and non-coding transcriptomic landscape of aortic complications in Marfan syndrome. Int J Mol Sci. 2024;25(13):7367.